
Stability Analysis of Directly Driven NIF Capsules

Introduction

In inertial confinement fusion (ICF), a spherical shell filled with a DT-gas mixture is compressed to high densities and temperatures to achieve ignition conditions.¹ Degradation from spherical symmetry during the implosion, however, limits the achievable compression ratios and could quench the ignition of the target. The main source of such asymmetry is hydrodynamic instabilities [such as Rayleigh–Taylor (RT)² and Bell–Plesset (BP)³ instabilities] seeded by both irradiation non-uniformities and target-fabrication imperfections. We have developed an analytical model to study stability of the direct-drive cryogenic NIF targets. The drive pulse for such targets consists of two distinct temporal regions (stages): the low-intensity (a few 10^{13} W/cm²) “foot” and the main drive (up to more than 10^{15} W/cm²). During the first stage, the laser energy is absorbed by the outermost layer of the target, heating up the shell material and launching a heat wave toward the pellet center. Material behind the heat front expands outwardly, creating an ablation pressure that induces the first shock wave propagating through the shell. Since the laser intensity in the first stage is constant in time and the equilibrium pressure behind the shock is uniform, the ablation front travels at constant velocity. In the absence of acceleration, the perturbations at the ablation front could grow due to the velocity and acceleration perturbations imposed by the laser-intensity modulations (“laser imprint”) and surface roughness [Richtmyer–Meshkov (RM)⁴ instability]. When the first shock breakout occurs at the rear surface of the DT ice, the pulse ramps up to the drive region (second or acceleration stage), launching the second shock. At this time, the ablation front starts to accelerate, creating conditions for the RT instability that magnify the perturbations seeded during the first stage. If the perturbation amplitude becomes too large during the shell acceleration, the shell breaks up and fails to reach ignition conditions. The shell integrity can be quantified by the “integrity factor” defined as $Y = A_{\text{mix}}/\Delta R$, where $A_{\text{mix}} \approx \sqrt{2}\sigma$ is the mix amplitude (bubble amplitude), ΔR is the shell thickness, and σ is the rms sum of the modes. The shell remains intact during the implosion if the integrity factor is less than unity for all time. At the end of the laser pulse, the shell starts to coast inward with

a constant velocity until the pressure of the DT-gas mixture becomes high enough to slow down the shell compression (beginning of the deceleration phase). During the deceleration phase the inner DT-ice surface is RT unstable. The growth due to this instability limits the compression ratios and increases the thermal conduction losses, reducing the total energy gain. Results from 2-D *ORCHID*⁵ simulations show that the gain reduction depends on the mode spectrum at the end of the acceleration stage. In this article we estimate the integrity factor during the acceleration phase and calculate the spectral distribution of the modes by using the results of the developed model and 2-D *ORCHID* simulations.

Seeding of RT Instability: Laser Imprint, Ablative RM Instability, and “Feedout”

As mentioned earlier, at the beginning of implosion, the ablation pressure launches a shock wave toward the target center. The surface roughness (due to the target fabrication imperfections) and also modulations in the laser intensity deform the shock front and generate perturbed velocity and acceleration fields inside the compressed region. During the shock transit time, the ablation front travels with a constant velocity, and the front perturbations could grow due to imposed velocity and acceleration perturbations.

1. Laser Imprint

Nonuniformities in the laser intensity cause different parts of the beam to ablate shell material at different rates, generating an ablation-pressure modulation along the ablation front. Since the shock speed scales as a square root of the shock strength, stronger shocks launched at the peak of ablation pressure propagate faster than shocks launched at the pressure valleys. The difference in the shock speeds distorts the shock front and creates a perturbed velocity field inside the compressed region. A velocity perturbation at the ablation front, in turn, leads to a linear-in-time front distortion growth $\eta \sim t$. Then, a rippled shock generates a lateral mass flow that leads to a pressure deficiency in the convex part (which protrudes the most into the uncompressed shell) and a pressure excess in the concave part of the shock front. This creates a pressure gradient that accel-

erates fluid elements, leading to an additional growth $\eta \sim t^2$. In ICF, however, several physical processes significantly reduce the imprint growth. First, as the heat front propagates into the cold portion of the target, material heats up and expands outwardly, creating a hot plasma corona. Thus, a finite zone (conduction zone) of hot plasma exists between the energy absorption region and the ablation front. Any pressure perturbations inside such a zone are reduced by the thermal conduction. The simplest theory⁶ (“cloudy day effect”) predicts that the pressure perturbations decay exponentially away from the critical surface $\tilde{p} \sim e^{-kx}$; thus, nonuniformities in the ablation pressure are reduced by a factor of e^{-kD_c} , where D_c is a distance between the absorption region and the ablation front, and k is the wave number corresponding to a specific mode of non-uniformity. An additional reduction in the imprint growth is due to the mass ablation. The main stabilizing mechanism produced by ablation is the dynamic overpressure or “rocket effect.”^{7,8} As a result, the imprint amplitude η_{imp} , which is defined as the amplitude of the ablation-front ripple calculated at the shock breakout time, takes the following form:⁹

$$\frac{\eta_{\text{imp}}}{\Delta R(\delta I_l/I_0)} \approx 0.4 \frac{A}{l} \hat{\eta} \left(e^{-\Delta_c} - e^{-2\Delta_a} \cos \Delta_{\text{bl}} \right) + \frac{e^{-2\Delta_a}}{\Delta_{\text{bl}}} \left(0.9 + 0.8 \frac{V_c}{c_s} \hat{\eta} \right) \sin \Delta_{\text{bl}} + \eta_v^{\text{imp}}, \quad (1)$$

where δI_l is the intensity modulation, I_0 is the average intensity,

$$\hat{\eta} = c_s^2 / (V_a V_{\text{bl}} + V_c^2),$$

$$\Delta_a = 2(l/A) V_a / c_s,$$

$$\Delta_{\text{bl}} = 2(l/A) \sqrt{V_a V_{\text{bl}}} / c_s,$$

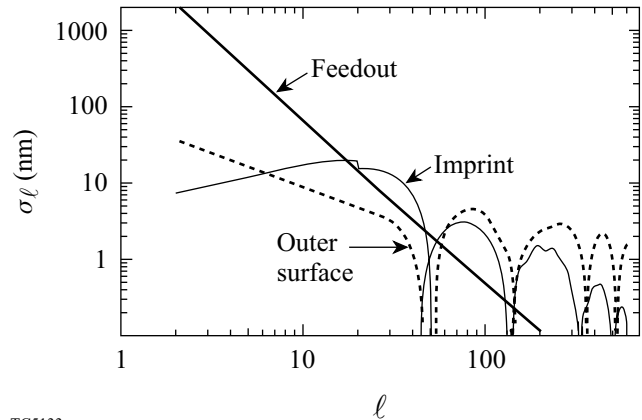
A is the shell’s in-flight aspect ratio, V_a and V_{bl} are the ablation and blow-off velocities, respectively, V_c is the velocity of the critical surface with respect to the ablation front, and c_s is the sound speed of the compressed material. The term η_v^{imp} is due to the vorticity convection from the shock front.

Using the analytical model of the RT instability (described later in the **Acceleration Phase** section), it is found that laser imprint alone can break up the shell during target acceleration and this can quench ignition; thus, an additional reduction in

imprint amplitude is critical for a successful implosion. A significant improvement in the beam uniformity has been made in recent years by introducing smoothing by spectral dispersion (SSD)¹⁰ and induced spatial incoherence (ISI)¹¹ smoothing techniques. To account for the intensity variation in a realistic laser pulse, SSD is modeled using the 2-D hydrocode *ORCHID*, where the intensity nonuniformities have been reduced by the factor $\sqrt{t_c/(t_c + 4t)}$. This gives on average a reduction in rms of laser nonuniformity $\sigma = \sqrt{t_c/t_{\text{avg}}} \sigma_0$, where the coherence time is taken to be

$$t_c = [\Delta v \sin(k\delta/2)]^{-1},$$

Δv is the bandwidth, t_{avg} is the averaging time, and δ is the speckle size. The result of 2-D *ORCHID* simulations (mode spectrum due to imprint (thin solid line) at the beginning of the acceleration phase) of the “all-DT” NIF target design¹² is plotted in Fig. 81.1. This result will be used later as an initial condition for the RT model.



TC5133

Figure 81.1
Mode spectrum at the beginning of the acceleration phase.

2. Outer-Surface Roughness

When the outer surface of the target is distorted, the ablation pressure launches a ripple shock at the beginning of implosion. The ripple shock, as discussed in the previous subsection, generates a lateral flow that leads to a perturbed pressure gradient and the perturbation growth. The theory describing the perturbation evolution at the corrugated ablation front driven by uniform laser irradiation has been described in Ref. 7. The theory shows that in the presence of ablation, the front perturbations oscillate in time with a damped amplitude. The main stabilizing mechanisms are the rocket effect and the vorticity

convection from the ablation front. Calculations⁷ show that the perturbation amplitude at the beginning of the acceleration phase normalized to the initial amplitude $\eta_0(l)$ can be written as

$$\frac{\eta^s}{\eta_0(l)} \approx \eta_v \left(\frac{2\Delta R}{c_s} \right) + \left\{ \frac{0.8c_s}{\sqrt{V_a V_{bl}}} \sin \Delta_{bl} - [0.1 + \eta_v(0)] \cos \Delta_{bl} \right\} e^{-2\Delta a}, \quad (2)$$

where the vorticity term $\eta_v(t)$ is defined in Ref. 7. Using Eq. (2) and taking the initial spectrum $\eta_0(l)$ from Ref. 12 (assuming surface finish of 840 Å), the mode spectrum due to a finite outer-surface finish is plotted in Fig. 81.1 (dashed line).

3. Inner-Surface Roughness (Feedout)

An additional seed of the RT instability is due to the rear-surface roughness that feeds out by the rarefaction wave generated at the first shock breakout time.¹³ The shock front first reaches the perturbation valleys, generating a rarefaction wave that starts to propagate toward the ablation front with the sound speed. By the time the shock reaches the perturbation peaks, the rarefaction wave originated at the perturbation valley has moved a finite distance, distorting the rarefaction wavefront. The peaks and valleys of the rarefaction wave travel at the sound speed, keeping the ripple amplitude constant. As the rarefaction wave breaks out of the shell, the ablation front starts to accelerate. Since the rarefaction front is distorted, however, there is a delay in accelerating the ablation front at the peaks and valleys. Because of such a delay, a finite velocity perturbation imprints at the ablation front, generating a seed for the RT instability. An additional seed (perturbation acceleration field) is created by the mass difference under the perturbation valleys and peaks. According to calculations,¹³ the feedout amplitude, $\eta^{f.o.}$, takes the following form:

$$\frac{\eta^{f.o.}}{\Delta_l} = \frac{0.06A}{l} + 0.15 \sqrt{\frac{A}{l}}, \quad (3)$$

where Δ_l is the initial rear-surface spectrum. Figure 81.1 shows mode spectrum due to feedout at the beginning of acceleration phase (thick solid line), assuming $\Delta_l \sim l^{-2}$ (Ref. 14) and initial total rms of the rear-surface modes $\sigma_r = 3 \mu\text{m}$.

Acceleration Phase

During the shell acceleration, the pressure and density gradients at the ablation front have opposite directions, creating a condition for the RT instability. In addition, because of the spherical convergence, the inner surface is subject to the BP instability. The RT and BP instabilities amplify the perturbations seeded during the first stage of the implosion.

Since the implosion of spherical shells is intrinsically unsteady (shell density, ablation velocity, and acceleration change in time), steady-equilibrium models cannot be used to study perturbation evolution, and a model for unsteady equilibria must be developed. The full system of conservation equations, however, is too difficult to be solved analytically. One of the simplifications that make the problem analytically tractable is an idealization of the ablation front as a surface of discontinuity [“sharp-boundary model” (SBM)]. The accuracy of such a model is compromised only when the mode wavelength is shorter than the ablation-front thickness L_0 . For ablators with small Froude numbers, such as CH or Be [the Froude number is defined as $V_a^2 / (gL_0)$, where g is acceleration], $L_0 \approx 0.1$ to $1 \mu\text{m}$; hence, for modes with the largest growth factors (the most damaging modes: $80 < l < 300$), the condition $kL_0 < 1$ is satisfied during the acceleration stage (assuming the minimum shell radius is $500 \mu\text{m}$). The density-gradient stabilization, nevertheless, can be included in simplified fashion by reducing the ablation-front acceleration by a factor $(1 + lL_m/R)^{-1}$, where L_m is the minimum density-gradient scale length and R is the shell radius. For ablation fronts with large Froude numbers, such as cryogenic DT, the unstable spectrum consists of only long-wavelength modes; thus, the SBM is valid in this case for all unstable modes. The model yields coupled differential equations describing the evolution of the outer and inner surfaces. The coefficients of these equations are functions of the ablation and the inner DT-ice interface trajectories and the ablation velocity that can be calculated using 1-D numerical simulations. To account for the nonlinear saturation, 3-D Haan’s model¹⁵ is applied after the mode amplitude reaches the saturation level $S(l) = 2R/l^2$. The accuracy of the developed RT model has been tested against 2-D *ORCHID* and *FCI2*¹⁶ simulations. For the most damaging modes, the prediction of the model is in good agreement with the numerical results.

The model shows that the shell remains intact during the implosion (the integrity factor is less than unity) if the laser nonuniformities are smoothed by 2-D SSD with the laser bandwidth larger than 0.3 THz, the outer-surface finish not exceeding $0.1 \mu\text{m}$, and the inner-surface finish $\sigma_r < 8 \mu\text{m}$ (assuming $\Delta_l \sim l^{-2}$). As shown in the next section, however,

the restriction on the minimum target gain imposes more stringent requirements for the irradiation uniformity and the surface finish.

Target Gain

As the shell accelerates inward, ablation-front perturbations grow due to the RT instability and feed through the shell approximately as $\eta_i(l) \approx \eta_a(l)(r_i/r_a)^l$, where $\eta_i(l)$ and $\eta_a(l)$ are the l -components of the inner- and ablation-surface amplitudes, respectively, and r_i and r_a are the inner- and ablation-surface radii. During the coasting and deceleration stages, the “feedthrough” grows, reducing the target compression ratio and limiting the ignition gain. To study the gain-reduction dependence on the mode spectrum, a series of 2-D *ORCHID* multimode simulations have been performed for an $\alpha = 3$ cryogenic NIF target design¹² with the distorted inner DT-ice interface. The initial power spectrum is taken in the form $\sigma_l = \sigma_0/l^\beta$ (Ref. 14), where σ_0 and β are the normalization constants. Since the spectrum of the inner-surface perturbations at the end of acceleration phase is heavily weighted toward the low mode numbers, the simulations have been performed for modes $2 < l < 50$ with the range of β and total rms 0 to 1.5 and 0.5 to 12 μm , respectively. The target gain is found to be a function of

$$\bar{\sigma} = \sqrt{0.06\sigma_{<10}^2 + \sigma_{\geq 10}^2},$$

where $\sigma_{<10}^2$ and $\sigma_{\geq 10}^2$ are rms nonuniformity of the modes below and higher than $l=10$. $\bar{\sigma}$ is calculated by using the inner-surface spectrum at the end of the acceleration phase. The simulation results are summarized in Fig. 81.2, where target gain is plotted versus $\bar{\sigma}$. Next, to take into account the laser imprint and surface roughness, the model described in the **Acceleration Phase** section is applied to the $\alpha = 3$ cryogenic NIF target design using the initial conditions derived in the **Seeding of RT Instability** section. Then, using both the derived mode spectrum and the result of Fig. 81.2, the target gain is plotted in Fig. 81.3 as a function of rear-DT-ice-surface finish and the laser bandwidth, assuming the initial outer-surface rms of 840 Å. Figure 81.3 shows that the yield reduction is less than 50% with respect to 1-D calculations if the inner-surface finish does not exceed 1.5 μm and the laser nonuniformities are smoothed by 1-THz, 2-D SSD.

Summary

An analytical model has been presented to study perturbation evolution at the ablation and inner surfaces of the imploding shell. The model describes the ablative Rayleigh–Taylor

and Bell–Plesset instabilities. The initial conditions for the model are determined by using existing theories of laser imprint, ablative Richtmyer–Meshkov instability, and feedout, and by performing a series of 2-D *ORCHID* simulations. The model and simulations showed that the direct-drive cryogenic $\alpha = 3$ NIF capsules remain intact during the implosion and the target gain is expected to be larger than 10 if laser nonuniformities are smoothed by 2-D SSD with the bandwidth $\Delta\nu > 0.5$ THz and inner-surface rms $< 1.5 \mu\text{m}$.

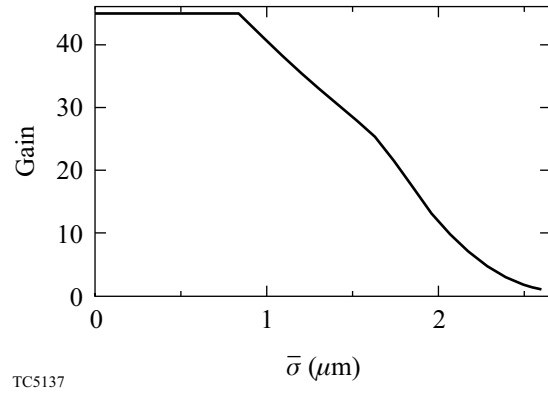


Figure 81.2
Plot of target gain G versus $\bar{\sigma}$.

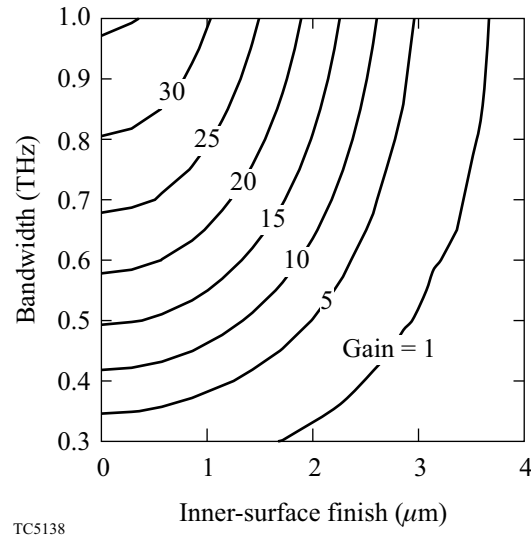


Figure 81.3
Plot of target gain versus initial rear-surface finish and laser bandwidth.

ACKNOWLEDGMENT

This work was supported by the U.S. Department of Energy Office of Inertial Confinement Fusion under Cooperative Agreement No. DE-FC03-92SF19460, the University of Rochester, and the New York State Energy Research and Development Authority. The support of DOE does not constitute an endorsement by DOE of the views expressed in this article.

REFERENCES

1. J. D. Lindl, *Inertial Confinement Fusion: The Quest for Ignition and Energy Gain Using Indirect Drive* (Springer-Verlag, New York, 1998).
2. Lord Rayleigh, in *Scientific Papers* (Cambridge University Press, Cambridge, 1900), Vol. II, p. 200.
3. M. S. Plesset, *J. Appl. Phys.* **25**, 96 (1954); G. I. Bell, Los Alamos National Laboratory, Report No. LA-1321 (1951).
4. R. D. Richtmyer, *Commun. Pure. Appl. Math.* **XIII**, 297 (1960).
5. R. L. McCrory and C. P. Verdon, in *Computer Applications in Plasma Science and Engineering*, edited by A. T. Drobot (Springer-Verlag, New York, 1991), pp. 291–325.
6. S. E. Bodner, *J. Fusion Energy* **1**, 221 (1981).
7. V. N. Goncharov *et al.*, *Phys. Rev. Lett.* **82**, 2091 (1999).
8. A. R. Piriz, J. Sanz, and L. F. Ibanez, *Phys. Plasmas* **4**, 1117 (1997).
9. V. N. Goncharov, S. Skupsky, P. W. McKenty, R. P. J. Town, T. R. Boehly, D. D. Meyerhofer, and O. V. Gotchev, “A Model of Laser Imprinting,” accepted for publication in *Physics of Plasmas*.
10. S. Skupsky, R. W. Short, T. Kessler, R. S. Craxton, S. Letzring, and J. M. Soures, *J. Appl. Phys.* **66**, 3456 (1989).
11. R. H. Lehmberg, A. J. Schmitt, and S. E. Bodner, *J. Appl. Phys.* **62**, 2680 (1987).
12. S. V. Weber, S. G. Glendinning, D. H. Kalantar, M. H. Key, B. A. Remington, J. E. Rothenberg, E. Wolfrum, C. P. Verdon, and J. P. Knauer, *Phys. Plasmas* **4**, 1978 (1997); Laboratory for Laser Energetics LLE Review **79**, 121, NTIS document No. DOE/SF/19460-317 (1999). Copies may be obtained from the National Technical Information Service, Springfield, VA 22161.
13. R. Betti, V. Lobatchev, and R. L. McCrory, *Phys. Rev. Lett.* **81**, 5560 (1998).
14. Laboratory for Laser Energetics LLE Review **79**, 131, NTIS document No. DOE/SF/19460-317 (1999). Copies may be obtained from the National Technical Information Service, Springfield, VA 22161.
15. S. W. Haan, *Phys. Rev. A* **39**, 5812 (1989).
16. E. Buresi *et al.*, *Laser Part. Beams* **4**, 531 (1986).

